International Journal of Heat and Fluid Flow 31 (2010) 442–449

Contents lists available at ScienceDirect

International Journal of Heat and Fluid Flow

journal homepage: www.elsevier.com/locate/ijhff

Wall shear stress measurement of near-wall flow over inclined and curved boundaries by stereo interfacial particle image velocimetry

Thien Duy Nguyen [a,*], John Craig Wells [a], Chuong Vinh Nguyen [b]

[a] Department of Civil and Environmental Engineering, Ritsumeikan University, 1-1-1 Noji Higashi, Kusatsu, Shiga, Japan
[b] Department of Mechanical and Aeronautical Engineering, Monash University, Vic. 3800, Australia

ARTICLE INFO

Article history:
Received 7 September 2009
Received in revised form 25 November 2009
Accepted 2 December 2009
Available online 15 January 2010

Keywords:
Stereo interfacial particle image velocimetry
Near-wall flow
Curved boundary
Wall shear
Backward-facing step

ABSTRACT

In investigations of laminar or turbulent flows, wall shear is often important. Nevertheless, conventional particle image velocimetry (PIV) is difficult in near-wall regions. A near-wall measurement technique, named interfacial PIV (IPIV) [Nguyen, C., Nguyen, T., Wells, J., Nakayama, A., 2008. Proposals for PIV of near-wall flow over curved boundaries. In: Proceedings of 14th International Symposium on Applications of Laser Technique to Fluid Mechanics], handles curved boundaries by means of conformal transformation, directly measures the wall gradient, and yields the near-wall tangential velocity profile at one-pixel resolution. In this paper, we show the feasibility of extending IPIV to measure wall gradients by stereo reconstruction. First, we perform a test on synthetic images generated from a direct numerical simulation (DNS) snapshot of turbulent flow over sinusoidal bed. Comparative assessment of wall gradients derived by IPIV, stereo-IPIV and particle image distortion (PID) [Huang, H.T., Fiedler, H.E., Wang, J.J., 1993. Limitation and improvement of PIV. Experiments in Fluids 15(4), 263–273] is evaluated with DNS data. Also, the sensitivity of IPIV and stereo-IPIV results to the uncertainty of identified wall position is examined. As a practical application of IPIV and stereo-IPIV to experimental images, results from turbulent open channel flow over a backward-facing step are discussed in detail.

© 2009 Elsevier Inc. All rights reserved.

1. Introduction

Measurement of wall shear gradient in laminar or turbulent flows is important. A measured wall shear distribution can facilitate understanding of the near-wall flow dynamics, e.g. coherent structures interacting with the wall, or flow separation. Turbulent energy production is associated with velocity shear, and is accordingly large in high shear gradient regions, which are often bounded by irregular boundaries. Flow systems with curved boundaries are commonly found in many engineering applications and in the environment. For example, in the field of river engineering, much effort has gone into finding relations among the wall shear stress, sediment transport and bed forms such as "ripples" and "dunes".

In experimental fluid mechanics, particle image velocimetry (PIV) is now the most common way to measure velocity. However, conventional PIV is usually difficult to apply to near-wall regions because of the low tracer density, high velocity gradient and strong wall reflection. Such problems are compounded when performing standard PIV next to inclined or curved boundaries.

To mitigate problems with the reliability and accuracy of conventional PIV measurements in high shear regions, Huang et al. (1993) proposed particle image distortion (PID). The method starts with a standard PIV cross-correlation, then deforms particle image template to compensate iteratively the particle displacements and achieves higher signal-to-noise ratio.

However, a drawback of PID is an increase in computation time during its iteration. Lecordier et al. (1999) presented an intermediate algorithm that based on an iterative sub-pixel translation and rotation of interrogation areas. In this work, the interrogation windows can be rotated in the local direction of displacement or shifted in fractions of pixel of the velocity magnitude previously estimated. This method could reduce undesirable effects of velocity gradients and the computation cost was about 3–6 times longer than the conventional PIV approach.

Adapting PID to a straight non-slip wall, Nguyen and Wells (2006b) proposed "PIV/ interface gradiometry (PIV/IG)". PIV/IG directly measures shear gradient at a wall by anchoring the first image template at the wall and shearing it parallel to the wall before cross-correlating with the second image template. The shear ratio yielding the maximal correlation coefficient is taken to be the measured velocity gradient. Superior to differentiation of conventional PIV data for measuring wall shear gradient, PIV/IG was however limited to the straight walls aligned with the sensor's pixel lines.

To completely exclude the contribution of wall interface from the correlation process, Theunissen et al. (2008) positioned,

* Corresponding author. Tel.: +81 080 5301 1530; fax: +81 77 561 3418.
E-mail address: gr044050@ed.ritsumei.ac.jp (T.D. Nguyen).

0142-727X/$ - see front matter © 2009 Elsevier Inc. All rights reserved.
doi:10.1016/j.ijheatfluidflow.2009.12.002

oriented and stretched the interrogation windows by a factor proportional to the number of particles in the image template. An increase in resolution and robustness of this algorithm were shown when utilized with the adaptively structured grid to the PIV images of flat-smooth wall.

To resolve the very near-wall flow near a curved boundary, Nguyen and Wells (2006a) proposed an image transformation followed by one-dimensional (1D) correlation of each pixel line parallel to the wall. Such image transformation can stretch an image segment above a curved wall into a rectangle. The 1D correlation is then implemented to produce a "correlation stack" that shows the tracer's tangential displacement versus wall-normal distance. The wall shear gradient and tangential velocity profile are determined from these correlation stacks. Nguyen et al. (2010) refined the algorithm for determining the tangential velocity profile. The combined method thus could yield near-wall profile of tangential velocity, not just wall gradient, and was accordingly renamed as "interfacial PIV". In that work, we validated IPIV with two-component (2C) synthetic images generated from direct numerical simulation (DNS) data.

In this paper, we present the extension of IPIV to stereo measurement of wall shear, denoted as stereo-IPIV (SIPIV), and consider its sensitivity to the accuracy of wall boundary detection. The structure of the paper is as follows. First, Section 2 reviews IPIV. In Section 3, synthetic images are generated from a DNS snapshot of a turbulent flow over a sinusoidal wall; orthogonal and oblique views yield 2C PIV images and stereo image pairs. Comparative assessment of wall gradients that result by applying IPIV and stereo-IPIV to these synthetic images is performed and benchmarked with the DNS data. In Section 4, as an application to a real flow, open flume tests with a backward-facing step (BFS) are presented. A combined system of two-component PIV (2CPIV) and stereo PIV (SPIV) has been implemented to examine the flow structure behind the step. Applications of IPIV and stereo-IPIV measurement to the experimental images are discussed.

2. Summary of interfacial PIV

A review of IPIV Nguyen and Wells (2006a) is presented in this section. First, we identify the wall boundary. Second, an image segment above the (curved) wall is stretched to a rectangle by means of an image transformation. The lower edge of such image template coincides with the wall boundary. Third, we calculate a stack of 1D correlation curves by cross-correlating each horizontal pixel line within the templates of the transformed images of the first and second exposures. Fourth, velocity gradient, extracted from the correlation stack, is integrated up from the wall one pixel at a time to yield a profile of tangential velocity Nguyen et al. (2010). Finally, a reverse transformation provides the physical values of wall gradient and tangential velocity profile.

2.1. Identifying wall boundary

In the image set, the wall position could be extracted by using a second-order derivative edge detection algorithm proposed by Marr and Hildreth (1980), named Laplacian of Gaussian. This algorithm is followed by deriving the second derivative of an intensity matrix after smoothing image with a Gaussian kernel. The raw wall positions then are detected by searching the zero-crossing points and smoothed by a low-pass filtering of a Fourier kernel. In Section 3.1, we will evaluate the performance of the second-order derivative detection algorithm versus the first-order derivative detection algorithm when applied to synthetic images. Fig. 1a exemplifies a detected boundary from the images of an open water channel flow over a sinusoidal wall.

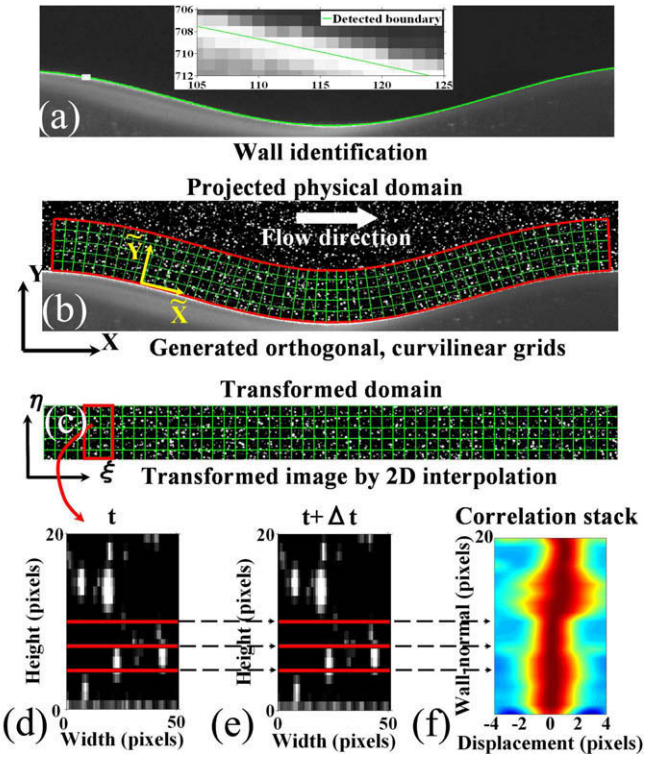

Fig. 1. Step 1 of IPIV: (a) wall identification. Step 2 of IPIV: (b) orthogonal, curvilinear grids are generated for conformal transformation; (c) transformed image by 2D interpolation. Step 3 of IPIV: line correlation applied to templates (d and e) yielding normalized correlation stack (f). The coordinates (X, Y) and $(\tilde{X}, \tilde{Y})$ in Fig. 1b indicate the pixel array and local coordinate systems, respectively; α is the angle between (X, Y) and $(\tilde{X}, \tilde{Y})$ coordinates.

Errors of the wall identification process can influence the accuracy of our measurement technique; when imposing the no-slip condition to help infer the wall gradient, the results are clearly sensitive to the assumed wall position. In Section 3.4, we will investigate the sensitivity of the IPIV and stereo-IPIV wall gradient measurements to errors in boundary identification.

2.2. Conformally transforming near-wall image region to rectangle

From the identified contour of boundary, we use SeaGrid, a Matlab Toolbox developed by Denham (2000) to generate an orthogonal curvilinear grid whose lower boundary lies on the detected wall (cf. Fig. 1b). The grid generation is based on the designated boundaries enclosing the curved region (red curves in Fig. 1b)[1] and the number of points segmented on each contour. Once the boundary points have been distributed, a Laplace equation solver fills in the interior of the domain with the curvilinear orthogonal grid lines to preserve right angles between two coordinates at every grid points. The orthogonal curvilinear coordinate system permits a conformal transformation between a complicated and curved region into a rectangular by using a system of equation mathematically described in Ives and Zacharias (1987).

The curved image segment, named physical domain (x, y), is then transformed into a rectangle, named transformed domain whose coordinates are denoted (ξ, η). The image intensities of the transformed template are produced by bicubic interpolation from corresponding intensities inside the grid region (cf. Fig. 1c).

[1] For interpretation of color in Fig. 1, the reader is referred to the web version of this article.

In our measurements, we use a local coordinate system $(\tilde{x},\tilde{y})$ to express the local wall flow properties, such as wall gradient and near-wall velocity. However, the orientation of such coordinate system varies with the slopes of the curved boundary. Thus, it is advantageous to compute the flow properties in the transformed domain and then reverse transform them to the physical domain.

In the present approach, the image transformation is limited to smoothly varying boundaries. In case of boundary with sharp corner, image strips could be defined and separately transformed. The benefits of our image transformation algorithm can be reviewed in Nguyen et al. (2010); wall shear gradients obtained by applying PID to the transformed synthetic images showed a better agreement to the original DNS data than those by applying the standard PIV with centroid shifting correction Hochareon et al. (2004) to the non-transformed synthetic images.

2.3. Calculating stack of line correlations

As designed to deal with near-wall flows, IPIV requires that the wall normal inter-frame tracer displacement be substantially less than particle image diameter. To satisfy this constraint, one can shorten the time delay between the first and second exposures. If this condition is satisfied, a purely tangential search can produce a correlation peak. We use a 1D correlation function, or line correlation, to produce a "stack" of 1D correlation curves. The covariance $C_{U,n}$ is calculated by cross-correlating an intensity distribution $I(m)$ along each line n on a template of the first exposure with the corresponding pixel line on a template of the second exposure,

$$C_{U,n}=\sum_{m=1}^{M}(I_{m+U,n}-\bar{I}_{U,n})\left(I'_{m,n}-\overline{I'_n}\right), \tag{1}$$

where (M,N) are the width and height, and (m,n) are the pixel coordinates of a template in the rectangular transformed image. $\bar{I}_{U,n}$ and $\overline{I'_n}$ are the mean intensities on each pixel line of the first and second templates. To increase the signal-to-noise ratio in the correlation stack, the covariance $C_{U,n}$ can be normalized with the r.m.s. of $(I_{m+U,n}-\bar{I}_{U,n})$ and the r.m.s. of $(I'_{m,n}-\overline{I'_n})$ can be used. However, care must be taken because this calculation may intensify the noise. Fig. 1f is an example of a normalized correlation stack $C_{U,n}$, with tangential displacement searching U (horizontal axis) and wall-normal position (vertical axis), obtained from a pair of image templates (d) and (e) of the transformed images. The sub-pixel interpolation with sampling rate of 0.1 pixel is implemented before correlation to reduce pixel-locking.

2.4. Measuring wall shear and integrating velocity profile

In Nguyen and Wells (2006a), the near-wall tangential velocity profile was returned by using a Gaussian or a spline fitting to the strong peaks' positions identified from a covariance stack (rather than to the normalized correlation stack). Such procedure, however, was sensitive to the peak identification. One of the main sources of errors was false but strong peaks. Besides, extrapolation and interpolation schemes were required to obtain the velocity vectors at all wall-normal positions.

In IPIV, the velocity gradient is directly extracted from the correlation stack and iterated upward from the wall. At position n $(n=0,1,\ldots,N)$, the velocity gradient $grad(n)$ is measured by fitting a straight line to the correlation stack, then searching for a corresponding slope which maximizes the Gaussian-weighted sum of correlation values, as shown in Eq. (2),

$$F(grad)\equiv\left[\frac{\sum_{y=-N}^{N}C_{U,y}\Omega(y-n)}{\sum_{y=-N}^{N}\Omega(y-n)}\right]. \tag{2}$$

The Gaussian-weighting function Ω, shown in Eq. (3), is vertically centered at the current position n,

$$\Omega(y-n)=exp\left[-\frac{(y-n)^2}{2\sigma^2}\right]. \tag{3}$$

In wall shear measurement, to impose the no-slip condition at the wall, we combine the correlation stack and its rotated copy around the wall. Fig. 2a shows the wall gradient measurement with the Gaussian weighting distribution Ω of $\sigma=7.07$ pixels (white dashed curve) overplotted on the correlation stack (top half) combined with its rotated image (bottom half). The fitting line (blue) is free to rotate around point O lying on the wall. Correlation values along the fitting line are accumulated with the Gaussian weighting function Ω. The slope of line corresponding to the maximum summation of correlation values is taken as the measured wall gradient.

Analogously, the velocity gradient $grad(n)$ is measured upward from the wall one pixel at a time $(n=1,2,\ldots,N)$. The tangential velocity profile is then determined by integrating the obtained values of $grad(n)$. Fig. 2b illustrates the velocity gradient measurement at $n=9$ pixels; the solid white curve shows an integrated velocity profile. The full tangential velocity profile is shown on the right side of Fig. 3.

2.5. Reverse transforming to obtain physical values

A reverse transformation is required to obtain the physical values of the velocity and wall shear gradient. The current version of IPIV can only measure the tangential displacement component U from the transformed image. Thus, the magnitude of the local-tangential displacement $\tilde{u}$ and wall shear gradient $\frac{\partial\tilde{u}}{\partial\tilde{y}}$ in the local coordinate $(\tilde{x},\tilde{y})$ can be obtained by

$$\tilde{u}=Ug_{\xi}=U\sqrt{\left(\frac{\partial X}{\partial\xi}\right)^2+\left(\frac{\partial Y}{\partial\xi}\right)^2}, \tag{4}$$

$$\frac{\partial\tilde{u}}{\partial\tilde{y}}=\frac{\partial U}{\partial\eta}\frac{g_{\xi}}{g_{\eta}}=\frac{\sqrt{\left(\frac{\partial X}{\partial\xi}\right)^2+\left(\frac{\partial Y}{\partial\xi}\right)^2}}{\sqrt{\left(\frac{\partial X}{\partial\eta}\right)^2+\left(\frac{\partial Y}{\partial\eta}\right)^2}}, \tag{5}$$

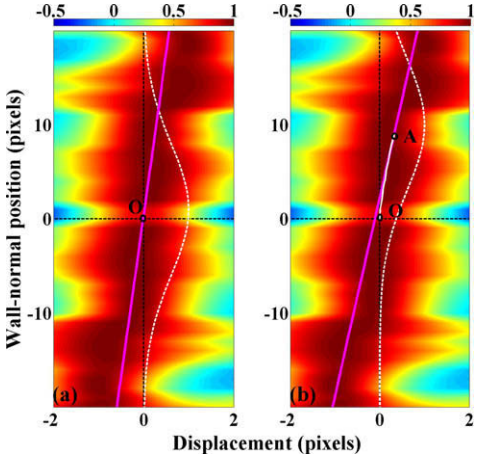

Fig. 2. Step 4 of IPIV: wall shear gradient and velocity measurements obtained from the same synthetic templates as Fig. 1d–f. Instantaneous normalized correlation stack (top half) is combined with its 180° rotated copy. Gaussian-weighted (white dash curve), line fitting (solid blue line) are overplotted. (a) Wall gradient measurement, (b) velocity gradient measurement at a point $n=9$ pixels. (For interpretation of the references to colour in this figure legend, the reader is referred to the web version of this article.)

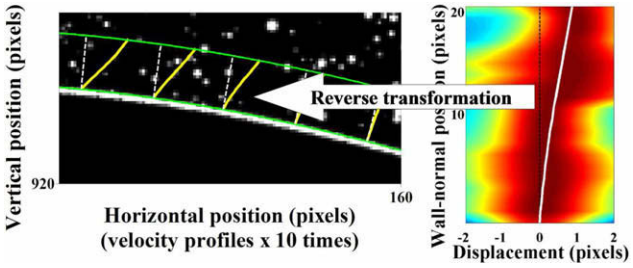

Fig. 3. Step 5 of IPIV: extracted IPIV profile (right) is reverse-transformed and overplotted (10×) on synthetic images (left).

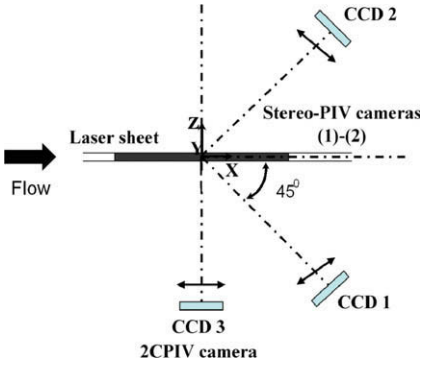

Fig. 4. Camera projections for generating synthetic images. Cameras lie at a distance equivalent to about 50 cm in vacuum from the center of the field of view, the height of which is 5.0 cm.

where $\frac{\partial U}{\partial \eta}$ is the wall shear gradient obtained from the transformed image. The g_ξ, g_η are the coefficients that characterize the conformal transformation. The left side of Fig. 3 shows a sample of tangential velocity profiles successfully produced by IPIV overplotted on a near-wall image region of synthetic image.

3. Stereo-IPIV; test with synthetic images

In order to test the IPIV algorithm in a stereo setup, a set of synthetic PIV image pairs has been generated from a DNS snapshot of a turbulent flow over a sinusoidal boundary Nakayama and Sakio (2002) and Yokojima (2002). The DNS computational domain consists of three wavelengths with 192 × 128 × 96 grid lines along the streamwise, spanwise and vertical directions. The ratio of the peak-to-peak amplitude to the wavelength is 0.1 yielding a maximum slope of 0.31. The Reynolds number Re_H defined by the bulk velocity U_m and the flow depth H is 6760, while that based on friction velocity and peak-to-peak height is 106. The present configuration has been chosen due to the availability of a DNS database, and because it can be compared to corresponding results from our previous work Nguyen et al. (2010). Results from this geometry can serve as a reference for configurations in which the angle of the wall, which respect to the viewing direction, lies within about 15°. One such configuration might be a diffuser or a smoothly varying backstep. In fact, the stereo configuration simulated here would present practical difficulty because the oblique cameras must view through the bed in order to image the illuminated wall over an entire wavelength; this would require perfect matching of refractive indices of the fluid and bed material. For 2C IPIV, this has been done in experiments of a model carotid artery by Buchmann et al. (2009). Because of the shallower incidence of rays passing through the solid–liquid boundary, the present configuration would be more challenging. A set of forty pairs of 1008 × 1008 pixel images are synthetically projected from a field of view of $H \times H$ ($H = 50$ mm) of the central wavelength. In the synthetic image generator, the particle image pattern and camera projection models proposed by Lecordier and Westerweel (2003) are implemented. Camera projections are sketched in Fig. 4. The camera magnification M is about 2/11, corresponding to about 1.05 wall units/pixel. This set includes 2CPIV images (perpendicular projection) and stereo PIV images (oblique projection). The laser sheet is specified as a Gaussian intensity profile with $\sigma = 0.5$ mm, or about 10 wall units. Tracers having non-uniform diameter are randomly scattered into a virtual 3D volume of the laser sheet. Image diameter of tracer has a Gaussian distribution with $\sigma = 1.28$ pixels, mean value of 2.8 pixels, and varies from 2.2 to 6 pixels. Seeding density in the generated images is about 0.01 particle/pixel. Besides, random background noise is also added with a Gaussian distribution with $\sigma = 2.5$. Based on the background levels from our experimental images, the minimum and maximum intensities of the generated noise are set at about 30 and 45 grayscale units, respectively. A time delay of $\triangle t = 1$ ms yields a maximal displacement of tracer of about 4.75 pixels. The image of the wall is synthesized by overlapping the intensities of particles lying on the specified boundary position. Boundary thickness is formed by oscillating these particles' positions vertically about 2 pixels. Fig. 5a shows a close-up of 2CPIV experimental image of turbulent flow over a wavy boundary, while Fig. 5b shows a correspondingly close-up of our 2CPIV generated synthetic image.

From the set of synthetic image pairs, we evaluate the relative performance of the first- and second-order derivative edge detection algorithms when applying to identify the wall boundary. Then, the extension of IPIV in wall shear measurement to stereo PIV applications (stereo-IPIV) is described. Next, the effectiveness of IPIV and stereo-IPIV are evaluated and compared with PID. In addition, the sensitivity of IPIV and stereo-IPIV to the uncertainty of wall position is also investigated.

3.1. Evaluation of the accuracy of wall identification algorithm

Edge detection is by far commonly applied in many applications, such as biomedical engineering, computer engineering, and ocean engineering...For monochrome images, most edge detection algorithms are based on one of two basic properties of the image intensity: discontinuity and similarity. In order to detect walls, we apply the two most common methods from the first category, which are the first- and second-order derivative algorithms.

The algorithm of the first-order derivative method is to calculate the gradient ∇f of the image intensity $f(x, y)$,

$$\nabla f = [G_x, G_y] = [\partial f/\partial x, \partial f/\partial y]. \quad (6)$$

where x and y are pixel coordinates. The magnitude of this vector is

$$|\nabla f| = \left[G_x^2 + G_y^2\right]^{1/2}. \quad (7)$$

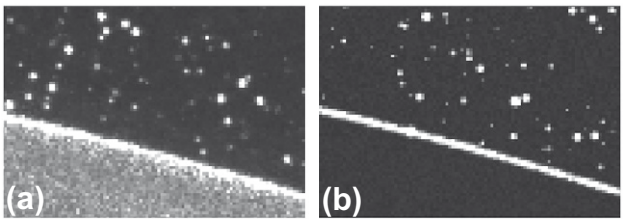

Fig. 5. Parts of 100 × 70 pixels from (a) 2CPIV experimental image and (b) 2CPIV generated synthetic image. Both are from turbulent flow over sinusoidal wall.

Such calculation can extract the coordinates (x,y) having the maximum rates of change in f. Points on the image edge are identified as the pixel coordinates where the gradient is greater than a specified threshold. In the other hand, the second-order derivative method commonly applies the Laplacian of $f(x,y)$

$$\nabla^2 f(x,y) = \frac{\partial^2 f(x,y)}{\partial x^2} + \frac{\partial^2 f(x,y)}{\partial y^2}. \tag{8}$$

The pixel coordinates of the boundary are then identified by finding the locations where $\nabla^2 f$ has zero crossings. The Laplacian operator, however, amplifies noise. Thus, it is necessary to implement the Laplacian operator in combination with other image processing techniques. For boundary identification, we first smooth the image $f(x,y)$ to reduce noise by using a Gaussian function $g(x,y)$, as follows:

$$s(x,y) = f(x,y) \otimes g(x',y'), \tag{9}$$

where $\otimes$ denotes convolution. Then, we evaluate the Laplacian of the smoothed image $s(x,y)$,

$$\nabla^2 s(x,y) = \nabla^2 (f(x,y) \otimes g(x',y')). \tag{10}$$

The Gaussian-smoothing function $g(x',y')$ is expressed as

$$g(x',y') = e^{-\frac{r^2}{2\sigma^2}}, \tag{11}$$

where $r^2 = x'^2 + y'^2$ and σ is the standard deviation whose value defines the degree of blurring if convolving the Gaussian operator with an image. Because of the linearity of the second derivative operator, it is equivalent to directly convolve the raw image with the Laplacian of the Gaussian, this translates to

$$\nabla^2 s(x,y) = f(x,y) \otimes \nabla^2 g(x',y'). \tag{12}$$

This algorithm is named "Laplacian of Gaussian" (LoG).

In order to select the appropriate edge detection technique, the two algorithms mentioned above are applied to our set of synthetic images. The threshold for the first-order algorithm is optimized as 0.05 while the values of the threshold and σ for the second-order algorithm are 3×10^{-4} and 2 (pixels), respectively. The detected raw wall positions are smoothed by using a Fourier kernel and compared with the correct values. The results show that the LoG algorithm yields a root mean square (r.m.s.) error of $\epsilon = 0.41$ pixels, which is superior to that of the first-order derivative algorithm with a r.m.s. error of $\epsilon = 1.04$ pixels. From our experience so far, the second-order edge detection technique appear to offer better results with images where a strong laser reflection is observed.

3.2. Stereo-IPIV: extension of IPIV to stereo PIV applications

To implement stereo-IPIV wall gradient measurement, we separately apply IPIV to the image captured by each of the oblique camera views. After wall identification, the orthogonal curvilinear grid is generated. The image transformation is then followed to stretch the curved image region above the wall into a rectangle. It is necessary to note that the stereo PIV cameras are viewing the illuminated fluid region through an oblique angle; the curved image segment inside the grid region then has a perspective distortion. However, the cameras in Fig. 4 are positioned sufficiently far to limit differences in magnification to less than 8%. Next, line correlation is executed on the templates of transformed images to yield the stack of 1D correlation curves. The wall gradient measurement is then performed on the obtained correlation stack. After reverse transformation, these projected wall gradients are applied to reconstruct the values of shear stress $\frac{\partial u}{\partial y}$ and $\frac{\partial w}{\partial y}$ by using Eq. (13) at physical positions, according to quasi-inversion of;

$$\begin{bmatrix} \frac{\partial U^{(1)}}{\partial y} \\ \frac{\partial V^{(1)}}{\partial y} \\ \frac{\partial U^{(2)}}{\partial y} \\ \frac{\partial V^{(2)}}{\partial y} \end{bmatrix} = \begin{bmatrix} \frac{\partial X^{(1)}}{\partial x} & \frac{\partial X^{(1)}}{\partial y} & \frac{\partial X^{(1)}}{\partial z} \\ \frac{\partial Y^{(1)}}{\partial x} & \frac{\partial Y^{(1)}}{\partial y} & \frac{\partial Y^{(1)}}{\partial z} \\ \frac{\partial X^{(2)}}{\partial x} & \frac{\partial X^{(2)}}{\partial y} & \frac{\partial X^{(2)}}{\partial z} \\ \frac{\partial Y^{(2)}}{\partial x} & \frac{\partial Y^{(2)}}{\partial y} & \frac{\partial Y^{(2)}}{\partial z} \end{bmatrix} \begin{bmatrix} \frac{\partial u}{\partial y} \\ \frac{\partial v}{\partial y} \\ \frac{\partial w}{\partial y} \end{bmatrix}, \tag{13}$$

where (x,y,z) and (X,Y) denote the physical and pixel coordinates, respectively, superscripts (1), (2) are the camera numbers used in the stereo PIV system. The equation of the stereo reconstruction of gradients, adapted by Nguyen and Wells (2006b), has the same form as that of the velocity reconstruction proposed by Soloff et al. (1997). Considering camera (1), derivatives on the left-hand side of Eq. (13) can be expressed in terms of measurable quantities as follows:

$$\begin{bmatrix} \frac{\partial U^{(1)}}{\partial y} \\ \frac{\partial V^{(1)}}{\partial y} \end{bmatrix} = \begin{bmatrix} \frac{\partial U^{(1)}}{\partial X} & \frac{\partial U^{(1)}}{\partial Y} \\ \frac{\partial V^{(1)}}{\partial X} & \frac{\partial V^{(1)}}{\partial Y} \end{bmatrix} \begin{bmatrix} \frac{\partial X^{(1)}}{\partial y} \\ \frac{\partial Y^{(1)}}{\partial y} \end{bmatrix}. \tag{14}$$

The four derivatives $\frac{\partial U^{(1)}}{\partial X}, \frac{\partial U^{(1)}}{\partial Y}, \frac{\partial V^{(1)}}{\partial X}$, and $\frac{\partial V^{(1)}}{\partial Y}$ can be obtained geometrically from the local wall gradient $\frac{\partial \widetilde{U}^{(1)}}{\partial \widetilde{X}}$ and $\frac{\partial \widetilde{U}^{(1)}}{\partial \widetilde{Y}}$ measured by IPIV in the local coordinate system $(\widetilde{X},\widetilde{Y})$. This translate the matrix on the right-hand side of Eq. (14) to

$$\begin{bmatrix} \frac{\partial \widetilde{U}^{(1)}}{\partial X} c^2(\alpha) - \frac{\partial \widetilde{U}^{(1)}}{\partial Y} s(\alpha)c(\alpha) & \frac{\partial \widetilde{U}^{(1)}}{\partial X} s(\alpha)c(\alpha) + \frac{\partial \widetilde{U}^{(1)}}{\partial Y} c^2(\alpha) \\ \frac{\partial \widetilde{U}^{(1)}}{\partial X} s(\alpha)c(\alpha) - \frac{\partial \widetilde{U}^{(1)}}{\partial Y} s^2(\alpha) & \frac{\partial \widetilde{U}^{(1)}}{\partial X} s^2(\alpha) + \frac{\partial \widetilde{U}^{(1)}}{\partial Y} s(\alpha)c(\alpha) \end{bmatrix}, \tag{15}$$

where α is the angle of the local coordinate $(\widetilde{X},\widetilde{Y})$ with respect to the pixel array (X,Y) (cf. Fig. 1b); $s(\alpha)$ and $c(\alpha)$ denote $\sin(\alpha)$ and $\cos(\alpha)$. Similarly, one can calculate the derivatives $\frac{\partial U^{(2)}}{\partial y}$ and $\frac{\partial V^{(2)}}{\partial y}$ for camera (2) to plug into the left-hand side of Eq. (13), which can be solved by least squares for the unknowns $\frac{\partial u}{\partial y}$ and $\frac{\partial w}{\partial y}$, analogously to stereo PIV.

It is important to consider the assumed constraint on apparently wall-normal inter-frame tracer displacement. In the case of 2CIPIV applications, the camera normally views in a direction nearly parallel to the wall, and thus tracer motion in the plane parallel to the wall, including motion out of the laser sheet's plane, does not project into an apparent wall-normal displacement. By contrast, stereo PIV configurations may not satisfy this assumption. Then tracer displacement in a plane parallel to the wall will yield an apparent wall-normal displacement on the images, in proportion to the sine of the viewing direction with respect to the wall's tangent plane. In the present virtual setup, the maximal value of this sine is about 0.22. Because the amplitude of spanwise motion is only moderate, this did not however lead to significant loss of signal. Such considerations constrain stereo-IPIV setups to a sufficiently small slope angle of the wall plane with respect to the viewing angles of the cameras in order to get tracer motions whose projections are nearly parallel to the projected intersection of the laser sheet with the wall.

3.3. Wall gradient comparisons of PID, IPIV and stereo-IPIV

This section describes a comparative assessment of wall gradient measurement by PID, IPIV and stereo-IPIV. Within this purpose, PID, IPIV and stereo-IPIV are all applied to the rectangular images that result from conformal transformation in step 2 of Section 2. Corresponding results of the wall shear gradient are compared with the true values of DNS to determine the accuracy of the processing techniques.

PID is performed on the transformed images at regular grid points. Its grid spacing is 5 pixels in vertical direction, equivalent to the distances from the first regular grid points towards the wall, and 25 pixels in horizontal direction. The interrogation window

size is 50 × 11 pixels to yield about 50% overlap between two horizontally or vertically adjacent windows. For the first grid points near the wall, the template height is reduced to 8 pixels to deal with the smaller displacements there. Also, a Gaussian-smoothing scheme analogous to step 4 of IPIV is applied to the velocity components in the horizontal and vertical directions, which reliably suppresses instability in PID iterations. Wall shear gradients of PID are computed by dividing the velocities at the first grid points by their distances towards the wall. In contrast, IPIV wall gradients are obtained directly from the correlation stacks (cf. Fig. 2). In addition, the wall gradient measurement by stereo-IPIV requires the stereo reconstruction as described in Section 3.2.

The obtained wall shear gradient is denoted as $\left(\frac{\partial u}{\partial y}\right)_i^j$ where i indexes the synthetic image sample ($P = 40$), and j indexes the measured streamwise station ($Q = 37$). The random error ϵ_{rand} and total error ϵ_{total} are calculated from PID, IPIV and stereo-IPIV results corresponding to the value of $\sigma = 7.07$ pixels or 7.4 wall units. The random error ϵ_{rand} is defined as the r.m.s. difference between $\left(\frac{\partial u}{\partial y}\right)_i^j$ and its ensemble-average $\overline{\left(\frac{\partial u}{\partial y}\right)^j}$,

$$\epsilon_{rand} = \sqrt{\frac{1}{PQ}\sum_{j=1}^{Q}\sum_{i=1}^{P}\left(\frac{\partial u^j}{\partial y_i} - \overline{\left(\frac{\partial u}{\partial y}\right)^j}\right)^2}. \tag{16}$$

The total error ϵ_{total} is defined as the r.m.s. difference between $\left(\frac{\partial u}{\partial y}\right)_i^j$ and the true value $\left(\frac{\partial u}{\partial y}\right)_S^j$ from DNS, namely

$$\epsilon_{total} = \sqrt{\frac{1}{PQ}\sum_{j=1}^{Q}\sum_{i=1}^{P}\left(\frac{\partial u^j}{\partial y_i} - \frac{\partial u^j}{\partial y_S}\right)^2}. \tag{17}$$

Fig. 6a shows the sample-average of wall gradients $\frac{\partial u}{\partial y}$ obtained by PID, IPIV and stereo-IPIV, benchmarked with true values of DNS. Wall shears measured by stereo-IPIV (circles) shows a better overall agreement with the DNS values (squares) than those by IPIV (triangles) and PID (diamonds). This trend is also observed in Table 1,

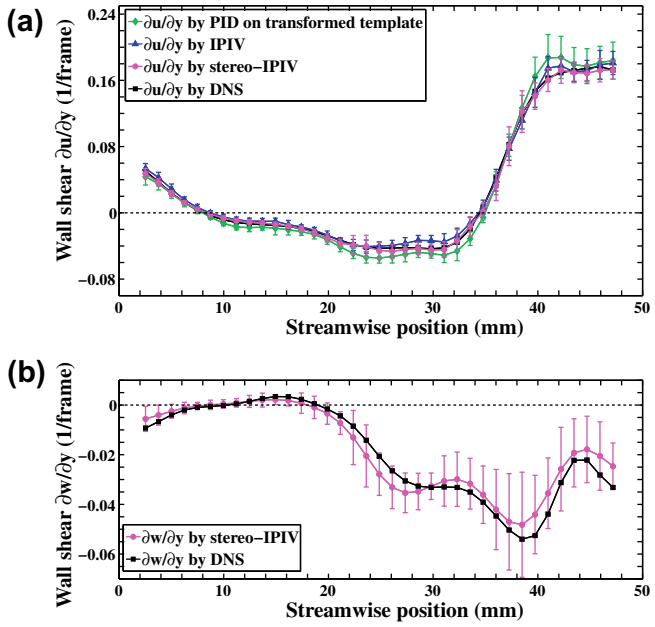

Fig. 6. Comparisons of wall shears derived from synthetic images with the Gaussian width of $\sigma = 7.07$ pixels or 7.4 wall units. (a) $\frac{\partial u}{\partial y}$ by IPIV (triangles) and stereo-IPIV (circles) are compared with PID (diamonds), and DNS (squares), (b) $\frac{\partial w}{\partial y}$ by stereo-IPIV (circles) is compared with DNS (squares). Half-height of error bar corresponds to standard deviation of measured values at each position.

Table 1
Random and total errors in $\frac{\partial u}{\partial y}$ of PID, IPIV and stereo-IPIV at precise wall position, for a Gaussian weighting width of $\sigma = 7.4$ wall units.

	PID	IPIV	Stereo-IPIV
ϵ_{rand} $(\triangle t^{-1})$	12.2×10^{-3}	8.2×10^{-3}	6.0×10^{-3}
ϵ_{total} $(\triangle t^{-1})$	16.7×10^{-3}	10.3×10^{-3}	9.7×10^{-3}

where stereo-IPIV has the smallest total error in comparing with PID and IPIV.

An advantage of stereo PIV is the capability to determine the out-of-plane component of velocity. Correspondingly, the reconstruction procedure of stereo-IPIV can extract the wall gradient $\frac{\partial w}{\partial y}$. Fig. 6b illustrates the sample-averaged wall gradient $\frac{\partial w}{\partial y}$ in comparison with DNS values. Analogously to Eqs. (16) and (17), the random and total errors of $\frac{\partial w}{\partial y}$ measurement have been calculated, yielding $(\epsilon_{rand}, \epsilon_{total}) = (4.6 \times 10^{-3}, 6.2 \times 10^{-3})$ $frame^{-1}$, about 10% and 15%, respectively, of the maximal value of the $\frac{\partial w}{\partial y}$ seen in the DNS profile.

3.4. Investigating the sensitivity of IPIV and stereo-IPIV to boundary positions

In Nguyen et al. (2006), we examined the sensitivity of wall shear results to the errors in detected boundary position when applying PIV/IG+ Nguyen and Wells (2006a) to the experimental images of a turbulent flow over a sinusoidal wall. In PIV/IG+, wall gradient was determined by fitting a straight line, with one point anchored at the wall, over a specified height h of the covariance stack (rather than normalized correlation stack in IPIV). Then, wall gradient was returned as the slope of the line maximizing the sum of interpolated covariance values over a limited fitting height, equivalent to a top-hat weighting scheme (versus a Gaussian-weighting scheme in the present version of IPIV). The principal conclusion was that the PIV/IG+ results were rather sensitive to errors in wall position (cf. similar analysis in Buchmann et al. (2009)).

In this subsection, we aim to investigate the effect of errors in wall location on the IPIV and stereo-IPIV results. For this purpose, the wall location is shifted by a value of y_w around the precise boundary; $y_w = -1$ and $y_w = 1$ indicate that the wall position is moved up and down 1 pixel, respectively. Then, the procedure of gradient determination described from Sections 2.2–2.5 is applied to the set of synthetic images to measure the wall shear gradients. The influence of the width σ of the Gaussian weighting scheme in Eq. (3) is considered. The random and total errors obtained with various values of σ at each boundary location are shown in Table 2. From Table 2, it is seen that an increase in the value of σ can clearly reduce the random error in wall gradient values measured by IPIV and stereo-IPIV. With the same value of σ implemented to the Gaussian-weighted scheme, stereo-IPIV measurement yields a better overall agreement to DNS data over IPIV, excepting the case of $y_w = -1$ where the assumed boundary is 1 pixel above the true wall position. For these test cases, $\sigma = 7.4$ wall units yields the smallest total errors for both IPIV and stereo-IPIV measurements. This observation concurs with the investigation of tangential velocity measurement in Nguyen et al. (2010). In addition, random and total errors of wall gradient $\frac{\partial w}{\partial y}$ with various values of y_w and σ are also included in Table 2. As the results of reconstruction procedure, the obtained wall gradient $\frac{\partial w}{\partial y}$ has likely suffered the errors of wall detection and the influence of Gaussian width σ.

It is worthy to note the robustness of our algorithms; the total errors from IPIV and stereo-IPIV measurements are fairly insensitive to the choice of the Gaussian width σ. The present data suggest

Table 2
Random and total errors in $\frac{\partial u}{\partial y}$ of IPIV, stereo-IPIV and $\frac{\partial w}{\partial y}$ of stereo-IPIV from synthetic images of sinusoidal wall for three offsets y_w in wall position.

		IPIV error		SIPIV error			
		$\partial u/\partial y$		$\partial u/\partial y$		$\partial w/\partial y$	
σ	y_w	$(\triangle t^{-1} \times 10^{-3})$		$(\triangle t^{-1} \times 10^{-3})$		$(\triangle t^{-1} \times 10^{-3})$	
(wall units)	(pixels)	ϵ_{rand}	ϵ_{total}	ϵ_{rand}	ϵ_{total}	ϵ_{rand}	ϵ_{total}
3.7	−1	9.9	12.9	9.4	14.0	6.8	9.5
	0	8.3	10.8	6.4	10.4	6.4	7.7
	+1	7.7	13.1	7.8	12.5	6.8	8.4
7.4	−1	9.6	12.5	9.5	13.8	4.7	9.3
	0	8.2	9.9	6.0	9.7	4.6	6.2
	+1	7.1	12.8	7.8	11.6	5.1	8.1
11.1	−1	7.5	12.1	9.0	13.9	4.0	9.2
	0	7.0	10.5	5.6	10.5	4.2	7.6
	+1	6.5	11.9	6.0	11.9	4.4	7.9

that σ should be specified near to the viscous sub-layer length scale, i.e. 5 wall units.

Notwithstanding the physical constraint of the non-slip condition at wall is indicated, the error of wall detection reduces the accuracy of IPIV and stereo-IPIV measurement; considerably when performing stereo-IPIV measurement 1 pixel above the precise boundary. The presence of movable tracer right on the assumed (incorrect) wall yields peak at the bottom of the correlation stack; and dominantly interferes the gradient determination with respect to the Gaussian weight scheme.

4. Flume test with backward-facing step

As an application of IPIV and stereo-IPIV to real images, experiment was performed in an open water channel with a backward-facing step. Experimental images were recorded by 2CPIV and stereo PIV systems. The 2CPIV used a Pulnix TM6710 charge couple device (CCD) camera with a resolution of 640×480 pixels of $9 \times 9\ \mu m^2$. Two Kodak ES1.0 CCD cameras comprised the stereo PIV; each has a full size of 1008×1018 pixels of $9 \times 9\ \mu m^2$. The water was seeded by hollow glass spheres with a mean diameter of $10\mu m$. The coordinate origin was situated at the step corner, with the streamwise, vertical and spanwise directions denoted by x, y and z, respectively. A double pulsed Nd:YAG laser was used to illuminate a 2 mm thick vertical sheet of the flow in the mid-plane of the test section. In the stereo PIV arrangement, viewing angle of cameras was set at 45° on either side of the channel from the downstream direction, analogously to Fig. 4. The camera bodies were slightly rotated to satisfy the Scheimpflug condition. Acquisition software was adapted in the LabView platform to control a PCI timer card for triggering the laser pulses and feeding signals.

In the experimental configuration , channel width and step height h were 50 cm and 16.5 mm, respectively. Reynolds number Re_h, based on the mean streamwise velocity U_0 and the step height h, was about 2800. The fluid region in the xy plane, with x/h ranging from 0.5 to 4.25, was imaged by the stereo PIV system while the 2CPIV camera was placed to record the particle images with x/h ranging from 4.5 to 7. Measured positions are sketched in Fig. 7. The time interval between the first and second exposures was $\Delta t = 3$ ms and sampling rate was set at 15 Hz. The number of measurement samples at each location was 3500. To acquire the wall shear, IPIV and stereo-IPIV were applied to a set of 3500 pairs of 2CPIV and stereo PIV experimental images at intervals of $0.25h$ along the streamwise direction.

The wall gradient $\frac{\partial u^{(i)}}{\partial y}$ with a superscript (i) denotes a value derived from an instantaneous line correlation stack of IPIV or stereo-IPIV. The ensemble-averaged wall shears by applying IPIV *(connected triangles)* and stereo-IPIV *(connected diamond)* are plotted

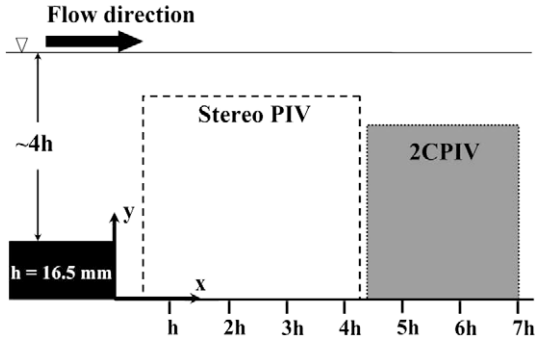

Fig. 7. Flume test with a backward-facing step.

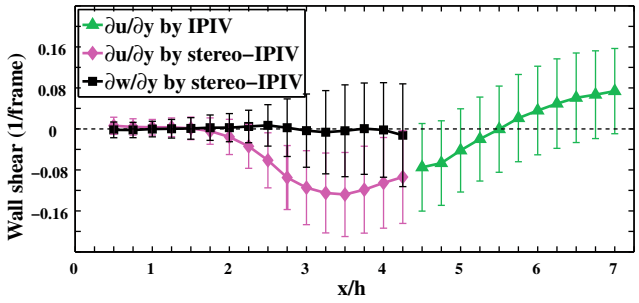

Fig. 8. Averaged wall gradients $\frac{\partial u}{\partial y}$ of IPIV (triangles), stereo-IPIV (diamonds) and $\frac{\partial w}{\partial y}$ of stereo-IPIV (squares) from BFS experiment. Half-height of bar corresponds to a standard deviation of the measured values at each position.

in Fig. 8. Half-height of error bar shows a standard deviation of the measured wall shears at each location. From the distributions of wall gradients along the streamwise direction, the mean reattachment length X_r can be identified as the streamwise location where the wall gradient becomes zero. From Fig. 8, a mean reattachment length of $X_r = 5.5h$ can be identified from the IPIV wall gradient curve.

In case of the wall shear measured by vector differentiation, a wall-normal resolution of measurement Δy is defined as the ratio of the distance from the first off-wall vector to the wall, divided by the step height h Piirto et al. (2007). For IPIV measurement, the wall-normal resolution Δy can be considered as the ratio between the Gaussian weighting width σ and the step height h. In this experiment, the value of σ is about 0.5 mm or 5.16 wall units, yielding $\triangle y = 0.03$. Compared to the resolution of $\triangle y$ about

Table 3
Overall r.m.s. fluctuations of IPIV and stereo-IPIV from BFS experiment.

	IPIV r.m.s.	SIPIV r.m.s.	
	$\partial u/\partial y(\triangle t^{-1}\times 10^{-2})$	$\partial u/\partial y(\triangle t^{-1}\times 10^{-2})$	$\partial w/\partial y(\triangle t^{-1}\times 10^{-2})$
y_w (pixels)	S	S	S
−1	8.4	6.4	6.5
0	8.3	5.7	5.8
+1	7.3	5.8	6.0

0.322 mm or 16 wall units Piirto et al. (2007), this high resolution is a considerable advantage of IPIV and stereo-IPIV in comparison with standard PIV in the near-wall region.

The overall r.m.s. fluctuations S of IPIV and stereo-IPIV results are calculated by

$$S=\sqrt{\frac{1}{KN}\sum_{k=1}^{K}\sum_{n=1}^{N}\left(\left(\frac{\partial u^{(i)}}{\partial y}\right)_k^n-\left(\overline{\frac{\partial u^{(i)}}{\partial y}}\right)_k\right)^2}, \tag{18}$$

where N is the number of image pairs, K is the number of measurement stations in the streamwise direction. The r.m.s. fluctuations S from the IPIV and stereo-IPIV wall gradient results, for different errors of wall detection, are shown in Table 3. The r.m.s. fluctuations vary significantly with the offset of boundary location. For example, moving the assumed wall position down by one pixel changes S by 1.0×10^{-2} and 0.7×10^{-2}, i.e., respectively, 12% of S for IPIV and stereo-IPIV.

In addition, the wall gradients $\frac{\partial w}{\partial y}$ are extracted using the reconstruction Eq. (13). The mean and r.m.s. fluctuations of the $\frac{\partial w}{\partial y}$ are overplotted in Fig. 8 as square symbols. It is seen that the mean values of $\frac{\partial w}{\partial y}$ vary only slightly around zeros. The reason is that the PIV measurement is performed at the middle plane of the channel width and the flow can be assumed as symmetry. As a result of the gradient reconstruction, the r.m.s. fluctuation S of $\frac{\partial w}{\partial y}$ suffers an effect of the uncertainty of wall location, i.e. one pixel offset yields about 14% of S.

5. Conclusions

In this paper, we have introduced the stereo-IPIV technique, which extends IPIV to stereo measurement of wall shear. We have also investigated the sensitivity of IPIV and stereo-IPIV to the accuracy of wall boundary detection. Synthetic images generated from a DNS snapshot of turbulent flow over a sinusoidal wall have been used to perform the comparative assessment of wall gradient measured by PID, IPIV and stereo-IPIV. The obtained results have shown that stereo-IPIV wall gradient measurement yields superior accuracy if the condition on apparent wall-normal tracer displacement on each camera image is satisfied. This condition constrains the inter-frame time delay and the angle between the wall and the viewing angles of stereo cameras. To resolve near-wall flows, the viscous sub-layer length scale is suitable for the width σ of the Gaussian-weighted scheme implemented in stereo-IPIV. This test has also shown that the errors in wall detection reduces the accuracy of the IPIV and stereo-IPIV wall gradient measurements.

Practical applications of IPIV and stereo-IPIV have been performed to a set of experimental images captured from open channel flow over backward-facing step. The distributions of mean wall gradients along the streamwise direction are measured; and the mean reattachment length can be determined with a high wall-normal resolution. An offset in the boundary position, added to estimate sensitivity to errors in wall detection, has a significant effect on the fluctuations of the measured wall gradients.

In future work, we expect to extend IPIV to measure the projected wall-normal velocity component from the correlation stack, by cross-correlating the pixel lines within the image templates in vertical direction. This will allow stereo-IPIV to obtain three components of near-wall velocity, in addition to the two components wall shear handled herein. Besides, it is desirable to implement the stereo-IPIV measurement in combination with the back-projection algorithm Coudert and Schon (2001), i.e. performing the stereo-IPIV procedure after dewarping raw PIV images. This procedure can systematically correct any small misalignment between calibration and measurement planes. Also, it will allow a uniform size and shape of the interrogation windows.

References

Buchmann, N., Jermy, M., Nguyen, C., 2009. Experimental investigation of carotid artery haemodynamics in an anatomically realistic model. International Journal of Experimental and Computational Biomechanics 1 (2), 172–192.

Coudert, S., Schon, J., 2001. Back-projection algorithm with misalignment corrections for 2D3C stereoscopic PIV. Measurement Science and Technology 12 (9), 1371–1381.

Denham, C., 2000. Seagrid orthogonal grid maker for matlab. <http://woodshole.er.usgs.gov/operations/modeling/seagrid/seagrid.html>.

Hochareon, P., Manning, K., Fontaine, A., Tarbell, J., Deutsch, S., 2004. Wall shear-rate estimation within the 50cc Penn State artificial heart using particle image velocimetry. Journal of Biomechanical Engineering 126 (4), 430–437.

Huang, H.T., Fiedler, H.E., Wang, J.J., 1993. Limitation and improvement of PIV. Experiments in Fluids 15 (4), 263–273.

Ives, D., Zacharias, R., 1987. Conformal mapping and orthogonal grid generation. AIAA, SAE, ASME, and ASEE, 23rd Joint Propulsion Conference, San Diego, CA.

Lecordier, B., Lecordier, J., Trinit, M., 1999. Iterative sub-pixel algorithm for the cross-correlation PIV measurements. In: Proceedings of the 3rd International Workshop on Particle Image Velocimetry (PIV 99), Santa Barbara, CA, September 1999.

Lecordier, B., Westerweel, J., 2003. The EUROPIV synthetic image generator (SIG). In: Stanislas, M., Westerweel, J., Kompenhans, J. (Eds.), Particle Image Velocimetry: Recent Improvements, pp. 145–162.

Marr, D., Hildreth, E., 1980. Theory of edge detection. Proceedings of the Royal Society of London. Series B, Biological Sciences, 187–217.

Nakayama, A., Sakio, K., 2002. Simulation of flows over wavy rough boundaries. Annual Research Briefs, Center for Turbulence Research, NASA Ames/Stanford University, 313–324.

Nguyen, C., Nguyen, T., Wells, J., 2006. Sensitivity of PIV/interface gradiometry to estimated wall position. Journal of the Visualization Society of Japan 26 (Suppl. 2), 203–206.

Nguyen, C., Nguyen, T., Wells, J., Nakayama, A., 2010. Interfacial PIV to resolve flows in the vicinity of curved surfaces. Experiments in Fluids, in press, doi:10.1007/s00348-010-0824-1.

Nguyen, C., Wells, J., 2006a. Development of PIV/interface gradiometry to handle low tracer density and curved walls. In: Proceedings of FEDSM2006 European Fluids Engineering Summer Meeting, FEDSM2006-98568, Miami, USA (2).

Nguyen, C., Wells, J., 2006b. Direct measurement of fluid velocity gradients at a wall by PIV image processing with stereo reconstruction. Journal of Visualization 9 (1), 199–208.

Piirto, M., Karvinen, A., Ahlstedt, H., Saarenrinne, P., Karvinen, R., 2007. PIV measurements in square backward-facing step. Journal of Fluids Engineering 129, 984.

Soloff, S., Adrian, R., Liu, Z., 1997. Distortion compensation for generalized stereoscopic particle image velocimetry. Measurement Science and Technology 8 (12), 1441–1454.

Theunissen, R., Scarano, F., Riethmuller, M., 2008. On improvement of PIV image interrogation near stationary interfaces. Experiments in Fluids 45 (4), 557–572.

Yokojima, S., 2002. Modeling and simulation of turbulent open- channel flows emphasizing free-surface effects. Ph.D. thesis, Kobe University, Japan.